

A thermo-mechanical phase field model considering solid-liquid transition: Application to electrothermal de-icing

Yuxuan Ying[1], Xudan Yao[1,2,*], Ye Feng[1,2] & Wei Huang[1,2]

[1]School of Aeronautics, Northwestern Polytechnical University, Xi'an, Shaanxi 710072, China
[2]National Key Laboratory of Strength and Structural Integrity, Xi'an, Shaanxi 710072, China
*Corresponding Author: x.yao@nwpu.edu.cn

Abstract

Electrothermal de-icing (ETDI) systems are utilized to preserve aerodynamic performance against icing threats, while the inherent de-icing mechanisms are yet to be accurately characterized via rigorous numerical modeling. In this study, an ETDI numerical framework based on a solid-liquid thermo-mechanical phase field model (PFM) is established. A typical fitting approach, namely thin plate spline method (TPSM), is employed to incorporate aerodynamic loads into modeling process. By studying an idealized de-icing example, it's validated that the coupling of aerodynamic forces and thermal stresses serve as the critical factor triggering ice fracture and shedding. Then, ETDI simulations on NACA 0012 wing leading edge indicate that a shorter icing time corresponds to a shorter de-icing time, and the ice shedding pattern is comparable to experimental results. It's verified that the "short-duration and high-power" heating scheme can achieve rapid de-icing with low energy usage, and the water film evolutions agree well with the empirical formula. Proposed work can help enrich the awareness of ETDI mechanisms and guide the design of ETDI systems.

Keywords: Electrothermal de-icing, thermo-mechanical analysis, phase field model, multi-physical modeling

1. Introduction

Aircraft icing may significantly affect the aerodynamic performance (e.g., reducing lift and increasing drag), thereby posing serious threats to flight safety and highlighting the importance of using ice protection system (IPS) [1]. Due to the advantages of stable control, enabling integrated molding and being compatible with electric aircraft [2,3], electrothermal IPS has gained widespread attention in recent decades. Capable of handling both anti-icing (preventing the ice accumulation) and de-icing (removing the existed ice) scenarios, electrothermal IPS has been installed on the wing leading edge of Boeing 787 [4] and the vertical stabilizer of Embraer Phenom 300E jet [5].

Although relevant investigations on the numerical modeling of ETDI have been conducted, they merely focused either on ice melting owing to temperature variation [6,7], or on the ice shedding associated with structural deformation [8,9]. To comprehensively understand the performance of ETDI, it's vital to explore the de-icing mechanisms. As mentioned in [10], during in-flight ETDI, stresses in the ice form from the combination of aerodynamic forces and thermal gradients, which may lead to the ice shedding before totally melted. This multi-physical process, including aerodynamic flow, solid-liquid transition and ice cracking, remains inadequately clarified, and the more refined modeling is required.

Based on fracture mechanics, different numerical methods have been used to study the ice shedding behavior [11,12]. Among them, the PFM, rooted in variational theory [13], has exhibited its superiority in addressing crack propagation and multi-physics frameworks, containing ice failure [14] and thermo-mechanical fracture [15]. This method also provides an innovative perspective for modeling ETDI. It's worth noting that, Bennani et al. [10,16,17] developed a series of ETDI models through PFM, which have been expanded to frameworks involving mixed-mode fracture and solid-liquid transition effects. Nevertheless, they neither discuss the temperature sensitivity of phase field length

scale, nor investigate the EDTI at wing leading edge.

Recently, we proposed a thermo-mechanical PFM incorporating solid-liquid transition, and the length scale for pure ice is determined by deriving a novel force-heat equivalent principle (FHEP) [18]. This model is validated against benchmark examples. In this context, the novel PFM will be combined with aerodynamic effects to further learn the in-flight ETDI mechanisms.

This paper is organized as follows: the solid-liquid PFM, accompanied with length scale derivation, is demonstrated in section 2. TPSM is employed in section 3 to address the transfer of aerodynamic loads at the fluid-solid interface. In section 4, numerical simulations of ETDI on idealized ice layer are conducted, and the contribution of aerodynamic forces to ice fracture is investigated. In section 5, the proposed model is applied to wing leading edge de-icing, and the effects of heating modes on energy consumption and water film thickness threshold are discussed. Finally, brief conclusions and perspectives finish this paper in section 6.

2. Solid-liquid thermo-mechanical PFM

Assuming a sharp crack surface Γ exists in a thermo-elastic body Ω, as shown in Fig. 1(a). By using phase field topology, the crack can be described by a scalar d, as illustrated in Fig. 1(b). The length scale l_0, which is positively correlated with damage gradient, is defined to quantify the degree of crack diffusion. Under the thermo-mechanical condition, Dirichlet boundaries for displacement and temperature fields are denoted as $\partial\Omega^b$ and $\partial\Omega^T$, while the corresponding Neumann boundaries yield $\partial\Omega^t$ and $\partial\Omega^q$. Q_h indicates the heat source term.

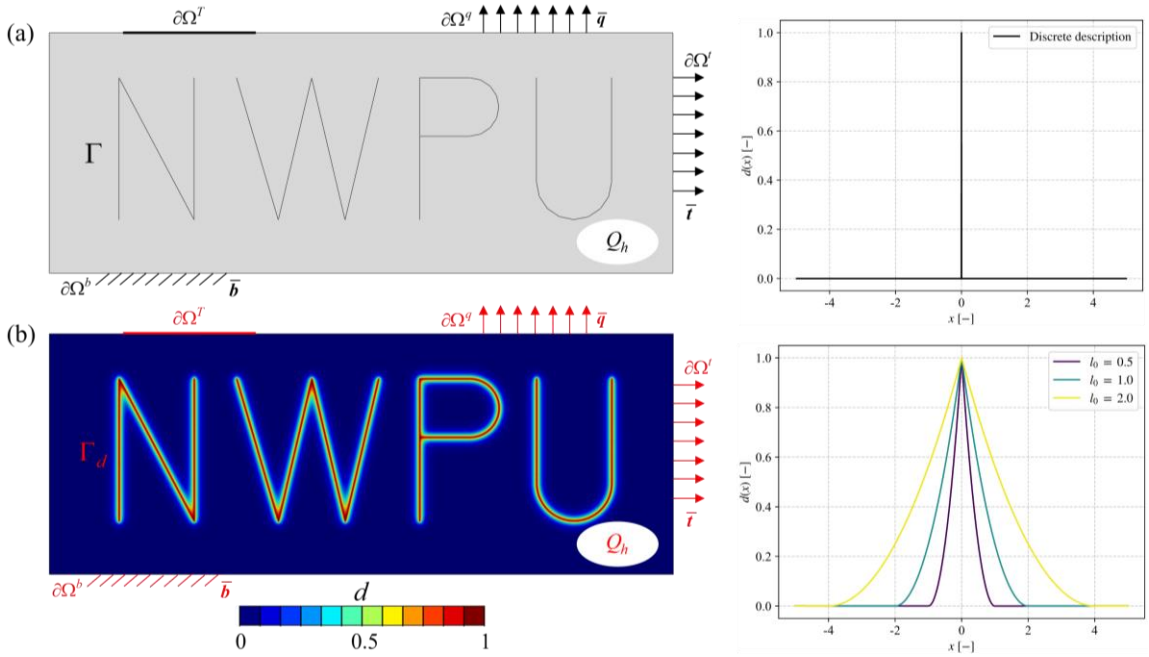


Fig. 1 Crack description within continuous media: (a) discrete crack, and (b) phase field crack.

2.1 Constitutive theory

2.1.1 Heat conduction modeling

The equivalent heat capacity method (EHCM) is introduced to address solid-liquid change problem. As a non-isothermal framework, the effective heat capacity C_e is defined to account for latent heat L during phase change, which reads:

$$C_e(T)=\left[1-\alpha(T)\right]C_s+\alpha(T)C_w+\frac{\mathrm{d}\alpha(T)}{\mathrm{d}T}L, \tag{1}$$

where C_s and C_w are the heat capacity for solid and liquid phases, respectively; $\alpha(T)$ denotes the phase fraction variable, which can be formulated in a first-order derivative-continuous form [18]:

$$\alpha(T)=\begin{cases}0 & \left(T<T_m-\Delta T,\ \text{solid zone}\right)\\ \operatorname{sgn}\left(T_m-T\right)\cdot\dfrac{\left(T-T_m\right)^2}{2\left(\Delta T\right)^2}+\dfrac{T-T_m}{\Delta T}+\dfrac{1}{2} & \left(T_m-\Delta T\le T\le T_m+\Delta T,\ \text{mushy zone}\right)\\ 1 & \left(T>T_m+\Delta T,\ \text{liquid zone}\right)\end{cases}, \tag{2}$$

where T_m is the melting point; $\alpha=0$ and $\alpha=1$ are solidus and liquidus line, respectively; ΔT reflects the range of phase transition interval.

Thus, the Fourier-type heat transfer equation reads:

$$\rho C_e(T)\dot{T}=k(\alpha)\nabla^2 T+Q_h, \tag{3}$$

where $\dot{*}$ indicates the time derivation of $*$; $k(\alpha)=k_s(1-\alpha)+k_w\alpha$ represents the mixed thermal conductivity; ρ is density, which is assumed to be identical for solids and liquids in this work.

2.1.2 Phase field fracture modeling

Under the small deformation scenario, elastic strain tensor $\boldsymbol{\varepsilon}_e$ reads:

$$\boldsymbol{\varepsilon}_e=\underbrace{\frac{1}{2}\left(\nabla\boldsymbol{u}+\nabla\boldsymbol{u}^{\mathrm{T}}\right)}_{\text{total strain tensor}}-\underbrace{\beta_t\left(T-T_0\right)\boldsymbol{I}}_{\text{thermal strain tensor}}, \tag{4}$$

where $\boldsymbol{u}$ is the displacement vector; β_t denotes the thermal expansion coefficient; T_0 indicates the initial temperature. For mechanical sub-problem, the quasi-static condition is assumed, resulting in the Lagrangian $\mathcal{L}$:

$$\mathcal{L}=\underbrace{\int_\Omega\bar{\boldsymbol{b}}\cdot\boldsymbol{u}\,\mathrm{d}V+\int_{\partial\Omega^t}\bar{\boldsymbol{t}}\cdot\boldsymbol{n}\,\mathrm{d}A}_{\text{external work}}-\int_\Omega\left\{\underbrace{f(\alpha)\left[g(d)\bar{\varphi}_+(\boldsymbol{\varepsilon}_e)+\bar{\varphi}_-(\boldsymbol{\varepsilon}_e)\right]}_{\text{elastic energy density}}+\underbrace{\frac{3G_c(T)}{8}\left(\frac{d}{l_0}+l_0\left|\nabla d\right|^2\right)}_{\text{fracture energy density}}\right\}\mathrm{d}V, \tag{5}$$

where $G_c(T)$ denotes the temperature-dependent fracture toughness; $\bar{\varphi}_+$ and $\bar{\varphi}_-$ are tensile and compressive strain energy, according to [19]; $f(\alpha)$ and $g(d)$ are two functions to capture the constitutive degradation induced by solid-liquid change and damage propagation. The empirical forms are adopted as follows:

$$f(\alpha)=(1-\alpha)^2,\ g(d)=(1-d)^2. \tag{6}$$

$\delta\mathcal{L}=0$ is required for arbitrary variational process, which yields:

$$\begin{aligned}\delta\mathcal{L}=&\int_\Omega\left[f(\alpha)g'(d)\bar{\varphi}_+(\boldsymbol{\varepsilon}_e)+\frac{8G_c(T)}{3}\left(\frac{1}{l_0}-2l_0\nabla^2 d\right)\right]\delta d\mathrm{d}V-\int_\Omega\left\{\bar{\boldsymbol{b}}+\nabla\left[f(\alpha)g(d)\bar{\boldsymbol{\sigma}}_+ +\bar{\boldsymbol{\sigma}}_-\right]\right\}\delta\boldsymbol{u}\mathrm{d}V+\\ &\int_{\partial\Omega}\left\{\frac{16G_c(T)l_0}{3}(\nabla d\cdot\boldsymbol{n})+\left[f(\alpha)g(d)\bar{\boldsymbol{\sigma}}_+ +\bar{\boldsymbol{\sigma}}_-\right]\delta\boldsymbol{u}\cdot\boldsymbol{n}-\bar{\boldsymbol{t}}\,\delta\boldsymbol{u}\right\}\mathrm{d}A\equiv 0\end{aligned}. \tag{7}$$

In addition, the two following constraints are introduced to improve the numerical model:

1. the hybrid scheme: the displacement equation is reconstructed via classical Cauchy stress tensor $\bar{\boldsymbol{\sigma}}$, to improve numerical stability;
2. Karsh-Kuhn-Tucker (KKT) condition: to avoid damage healing in solid region, a history variable $\mathcal{H}$, namely the maximum damage driving force, is used to modify phase field equation.

Thus, reconsidering Eq. (7), the coupled equation can be derived as:

$$\begin{cases} \nabla\cdot f(\alpha)g(d)\bar{\boldsymbol{\sigma}}+\bar{\boldsymbol{b}}=0 & \text{(Displacement field)} \\ 6G_c(T)l_0^2\nabla^2 d=8l_0 g'(d)f(\alpha)\mathcal{H}+3G_c(T) & \text{(Phase field)} \end{cases}. \tag{8}$$

2.1.3 Summary of governing equations

The final governing equations for the newly developed PFM are provided in Table 1, with the interconnection diagram between different fields presented in Fig. 2. In this work, ice is deemed to be isotropic, and following assumptions are raised to simplify the ETDI simulations:

(1) continuous ice accretion on the surface during ETDI is neglected;

(2) melted water layer is treated as inviscid, incompressible fluid;

(3) potential refreezing of overflow is excluded from the modeling process.

Table 1 Thermo-mechanical PFM considering solid-liquid transition.

Physical field	Governing equation	Boundary conditions
Displacement	$\nabla\cdot f(\alpha)g(d)\bar{\boldsymbol{\sigma}}+\bar{\boldsymbol{b}}=0$	$\boldsymbol{u}=\boldsymbol{u}^*$, $\boldsymbol{\sigma}\cdot\boldsymbol{n}=\bar{\boldsymbol{t}}$
Temperature	$\rho C_e\dot{T}=k(\alpha)\nabla^2 T+Q_h$	$T=T^*$, $\boldsymbol{q}\cdot\boldsymbol{n}=\bar{\boldsymbol{q}}$
Damage	$6G_c(T)l_0^2\nabla^2 d=8l_0 g'(d)f(\alpha)\mathcal{H}+3G_c(T)$	$d=d^*$, $\nabla d\cdot\boldsymbol{n}=0$

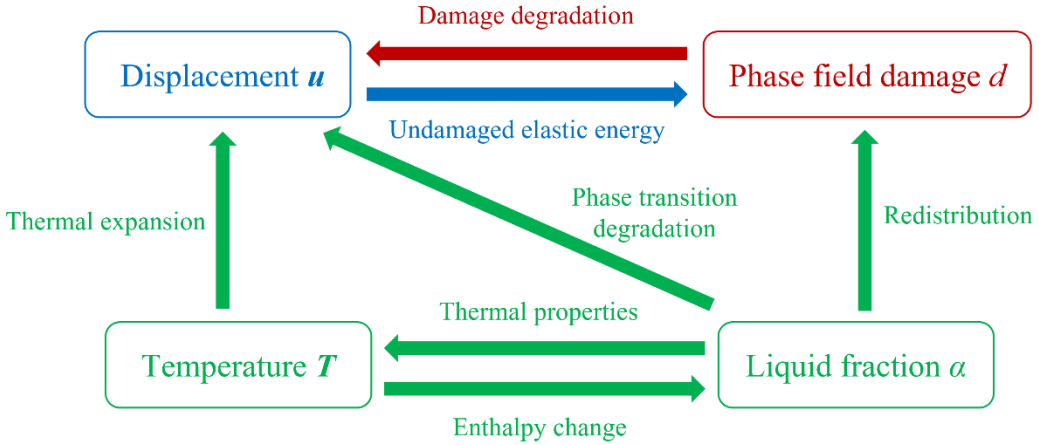


Fig. 2 Interconnections between different physical fields.

2.2 Length scale determination

Served as a material parameter, selection of length scale l_0 is crucial in numerical modeling. By applying $d\equiv 0$ (i.e., damage initiation condition) in Eq. (8), one can read:

$$l_0=\frac{3G_c(T)}{16f(\alpha)\varphi_c(T)}, \tag{9}$$

where $\varphi_c(T)=\sigma_c^2(T)/2E(T)$ represents the critical strain energy density (CSED); $\sigma_c(T)$ and $E(T)$ are temperature-dependent ultimate strength and young's modulus, respectively. It can be concluded that once $\varphi_c(T)$ and $G_c(T)$ are determined explicitly, l_0 can be calculated.

The key issue evolves into how to accurately describe the temperature-dependent CSED, and one effective method for this purpose is the FHEP. Developed by Li et al. [20], FHEP can help characterize the relationship between thermal energy and CSED, which has been applied to ceramics [21], composites [22], etc. Its standard form is given as:

$$\varphi_\kappa=K\int_0^T C_p\mathrm{d}\tau+\varphi_c(T), \tag{10}$$

where φ_κ is a constant which represents the energy storage; K describes the conversion between different energy term. It should be noted that $\varphi_c(T_m)\equiv 0$, leading to the expression of K:

$$K\int_0^{T_r} C_s \mathrm{d}\tau + \varphi_c(T_r) = K\int_0^{T_m} C_s \mathrm{d}\tau \Rightarrow K = \frac{\varphi_c(T_r)}{C_s(T_m - T_r)} \quad \text{(Conventional scheme)}, \tag{11}$$

where T_r is the reference temperature.

To including the latent heat effects, the EHCM can be incorporated. Assuming that $\varphi_c(T_m+\Delta T)\equiv 0$, Eq. (11) can be modified as:

$$\hat{K}\int_0^{T_r} C_s \mathrm{d}\tau + \varphi_c(T_r) = \hat{K}\int_0^{T_m+\Delta T} C_e \mathrm{d}\tau \Rightarrow \hat{K} = \frac{\varphi_c(T_r)}{C_s(T_m - T_r) + \Delta T C_w + L} \quad \text{(Enhanced scheme)}, \tag{12}$$

where $\hat{K}$ is the equivalent coefficient for enhanced FHEP. Thus, for an arbitrary T, its CSED can be derived by substituting Eqs. (11) and (12) into Eq. (10):

$$\begin{cases} \varphi_c(T) = \varphi_c(T_r)\left(1 + \dfrac{T_r - T}{T_m - T_r}\right) & \text{(Conventional scheme)} \\ \varphi_c(T) = \varphi_c(T_r)\left[1 + \dfrac{C_s T_r - \int_0^T C_e(\tau)\mathrm{d}\tau}{C_s(T_m - T_r) + \Delta T C_w + L}\right] & \text{(Enhanced scheme)} \end{cases}. \tag{13}$$

Eq. (5) means that, when T_r and $\varphi_c(T_r)$ are given (e.g., extracted from experimental data), CSED covering solid, transition and liquid regions can be automatically derived by using the thermophysical properties. The evolution of length scale can also be formulated by substituting Eq. (13) into Eq. (9).

Our previous work [18] has demonstrated that the enhanced FHEP can more accurately capture the CSED of ice layer. As already calibrated, $l_0 \approx 0.5\mathrm{mm}$ is utilized for ice.

3. Equivalent mapping of aerodynamic forces

To account for in-flight de-icing situation, aerodynamic pressure is incorporated into the numerical framework. As mentioned in Fig. 3, the nodes on fluid-ice interface are generally mismatched. Thus, to address the projections of aerodynamic forces, thin-plate spline method (TPSM) is employed.

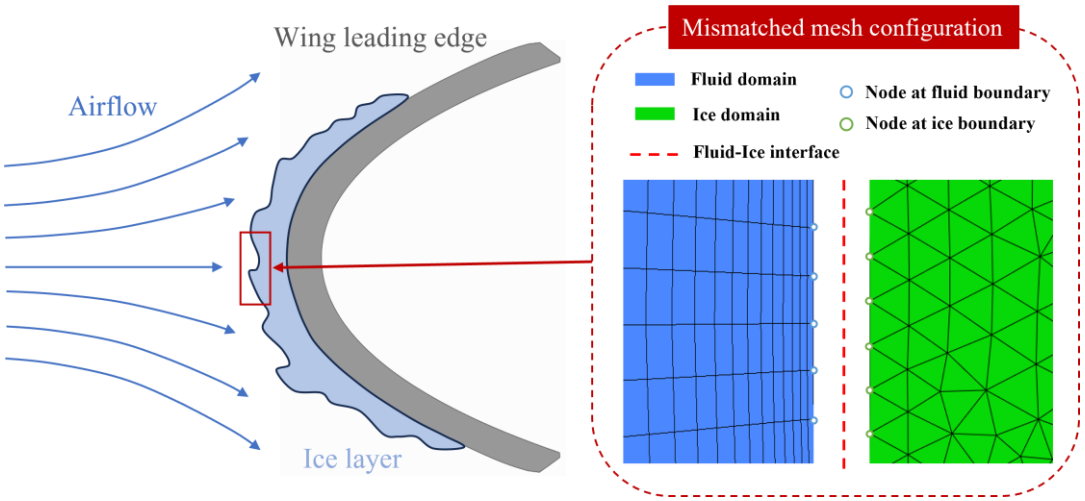


Fig. 3 mismatched interfacial mesh for ETDI.

Supposing the coordinate vectors of grid in fluid and solid domains are denoted as $\boldsymbol{X}_i$ and $\boldsymbol{X}_k$, respectively. The predicted pressure at $\boldsymbol{X}_k$ can be written by an approximate function W:

$$W(\boldsymbol{X}_k) = c_1 + \sum_{p=1}^{N} c_{p+1} X_k^p + \sum_{i=1}^{n} c_{N+1+i} r_i^2 \ln\left(r_i^2 + \phi\right), \tag{14}$$

where ϕ is a fitting parameter that generally assumes distinct values for surfaces with different properties; N is dimension; n is the number of interfacial grids in fluid domain. c_1, c_2, …, c_{N+1+n} are the weights of the radius basis function $\chi(r)=r^2\ln(r+\phi)$, and can be calculated through:

$$\begin{cases} \sum_{i=1}^{n} c_{N+1+i} = 0 \\ \sum_{i=1}^{n} c_{N+1+i} X_i^p = 0 \qquad (m=1,2,...,n \text{ and } m\neq i), \\ c_1 + \sum_{p=1}^{N} c_{p+1} X_m^p + \sum_{i=1}^{n} c_{N+1+i} r_{mi}^2 \ln\left(r_{mi}^2+\phi\right) + h_m c_{N+1+m} = W_m \end{cases} \tag{15}$$

where h_n is the weight coefficient of nth node, and is supposed to be close to 0. The interpolation radius, namely Euclidean distance, can be defined as:

$$r_{mi} = \sqrt{\sum_{p=1}^{N}\left(X_m^p - X_i^p\right)^2}\,. \tag{16}$$

TPSM is essentially implemented via solving a matrix equation $\boldsymbol{AC}=\boldsymbol{F}$, whose components read:

$$\boldsymbol{A}=\begin{bmatrix} \boldsymbol{0} & \boldsymbol{S} \\ \boldsymbol{S}^{\mathrm{T}} & \boldsymbol{Y} \end{bmatrix},\ \boldsymbol{C}=\begin{Bmatrix} c_1 & \cdots & c_{N+1} & c_{N+2} & \cdots & c_{N+1+n} \end{Bmatrix}^{\mathrm{T}},\ \boldsymbol{F}=\begin{Bmatrix} 0 & \cdots & 0 & W_1 & \cdots & W_n \end{Bmatrix}^{\mathrm{T}}, \tag{17}$$

with the detailed expression yields:

$$\boldsymbol{S}=\begin{bmatrix} 1 & 1 & \cdots & 1 \\ X_1^1 & X_2^1 & \cdots & X_n^1 \\ X_1^2 & X_2^2 & \cdots & X_n^2 \\ \vdots & \vdots & \vdots & \vdots \\ X_1^N & X_2^N & \cdots & X_n^N \end{bmatrix},\ \boldsymbol{Y}=\begin{bmatrix} h_1 & r_{12}^2\ln\left(r_{12}^2+\phi\right) & \cdots & r_{1n}^2\ln\left(r_{1n}^2+\phi\right) \\ r_{21}^2\ln\left(r_{21}^2+\phi\right) & h_2 & \cdots & r_{2n}^2\ln\left(r_{2n}^2+\phi\right) \\ \vdots & \vdots & \ddots & \vdots \\ r_{n1}^2\ln\left(r_{n1}^2+\phi\right) & r_{n2}^2\ln\left(r_{n1}^2+\phi\right) & \cdots & h_n \end{bmatrix}. \tag{18}$$

Therefore, once the pressure distribution and coordinates on fluid mesh are obtained, aerodynamic loads can be mapped onto the solid mesh, and further converted into nodal forces via shape functions. In this work, $N=2$ always holds.

In this study, planar triangular elements are adopted to discretize the computational domain. After deriving the pressure distribution, the nodal forces can be calculated by using shape functions:

$$\begin{bmatrix} F_{x,i} \\ F_{y,i} \\ F_{x,j} \\ F_{y,j} \end{bmatrix} = \frac{t_{ele}}{6}\begin{bmatrix} 2\left(y_j-y_i\right) & y_j-y_i \\ 2\left(x_i-x_j\right) & x_i-x_j \\ y_j-y_i & 2\left(y_j-y_i\right) \\ x_i-x_j & 2\left(x_i-x_j\right) \end{bmatrix}\cdot\begin{bmatrix} p_i \\ p_j \end{bmatrix}, \tag{19}$$

where i and j are two adjacent nodes within an element; x and y are horizontal and vertical coordinates, respectively; t_{ele} is the element thickness, and is set as 1.0 for plane problem.

4. Verification case: idealized ETDI on a flat plate

4.1 Setup of calculation condition

The aforementioned solid-liquid PFM, accompanied with TPSM-based projection of aerodynamic forces, is used to study ETDI on flat plate initially.

As illustrated in Fig. 4, the geometric configuration of the idealized ice block is characterized by the typical NACA 0019 aerodynamic profile. The convective heat transfer condition is imposed on the outer boundary of ice layer, with the coefficient set as $h=400\mathrm{W/(m^2\cdot K)}$. According to [10], the ice-

plate surface is assumed to be perfectly bonded, and heat flux is assigned to 72% area of the interface. Under the action of outer pressure and thermal stress, through-crack will generate and split the ice into two pieces [10].

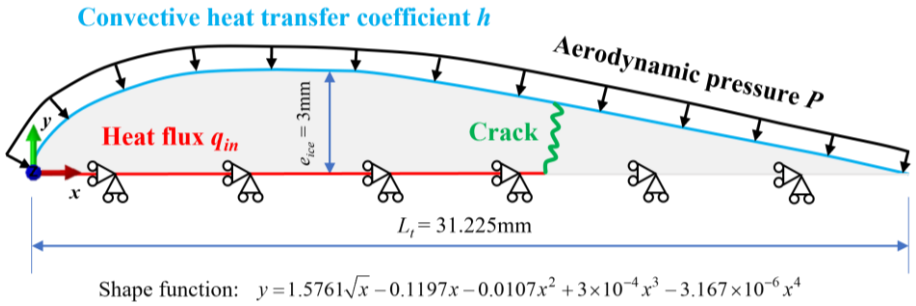


Fig. 4 Geometric shape and boundary conditions for idealized ice layer.

The aerodynamic parameters are stated in Table 2. Thermal and mechanical properties for ice are provided in Table 3 and Table 4, respectively. Unless otherwise stated, plane stress condition is adopted in the rest of the paper.

Table 2 Input parameters for solving flow field.

Variable	Re	V_∞*	T_∞*	P_∞*	AOA*
Value	2.08×10^5	136	263.15	61640.0	0
Unit	-	m/s	K	Pa	°

Notes*: V_∞, T_∞ and P_∞ are the velocity, temperature and pressure at far-field, respectively; AOA denotes the angle of attack.

Table 3 Thermophysical parameters for ice [18].

Variable	T_m	ΔT	C_s	C_w	k_s	k_w	L	ρ
Value	273	0.5	1762	4226	2.22	0.56	3.34×10^5	1000
Unit	K	K	J/kg/K	J/kg/K	W/m/K	W/m/K	J/kg	kg/m^3

Table 4 Mechanical parameters for ice [18].

Variable	$E(T)$	$K_{IC}(T)$*	l_0	β_t
Value	$9\left[1-1.42\times10^{-3}(T-238)\right]$	$\sqrt{10^{-9}\cdot(-0.183T+55.853)}$	5×10^{-4}	4×10^{-5}
Unit	GPa	$GPa\cdot m^{1/2}$	m	K^{-1}

Notes*: $K_{IC}(T)$ denotes the temperature-dependent stress intensity factor.

4.2 Validation of TPSM

The structured mesh of external flow field is shown in Fig. 5(a), where the boundary layer is generated following $y^+<1$. The Spalart-Allmaras (S-A) model [23] is adopted to account for turbulent effects.

The aerodynamic pressure distribution around the ice layer is illustrated in Fig. 5(b). A relative high-pressure region is visible near the stagnation point, corresponding to the location where the incoming flow is decelerated to near-zero velocity. The flow then accelerates, resulting in a pronounced low-pressure zone on the upper surface. A comparison with the numerical results reported in [16] is presented in Fig. 5(c), which proves the accuracy of flow field calculations.

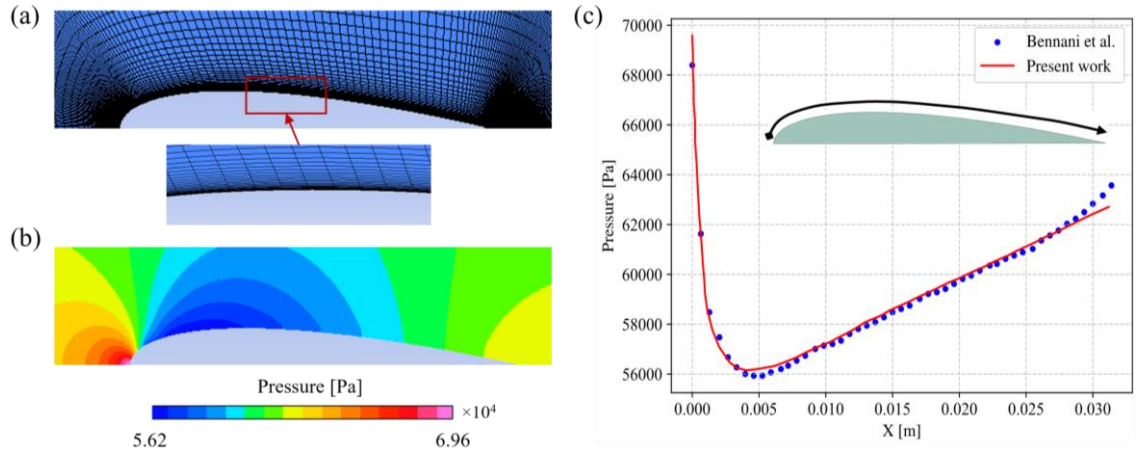


Fig. 5 Flow field calculations for idealized ice layer: (a) grid configuration, (b) pressure profile, and (c) comparison with the results reported by Bennani et al.[16].

Then, the effectiveness of TPSM is verified. The minimum size of solid element within the ice domain is approximately $h_{\min} \approx 5\times10^{-5}\,\mathrm{m}$, which satisfies the relation $l_0 \approx 10h_{\min}$. Three values of ϕ, i.e., 1×10^{-1}, 1×10^{-3} and 1×10^{-6}, are adopted, and the fitting performance of TPSM under each case is illustrated in Fig. 6. It can be concluded that as ϕ decreases, results of TPSM are in better agreement with numerical ones. When $\phi = 1\times10^{-6}$, the fitting result is satisfactory.

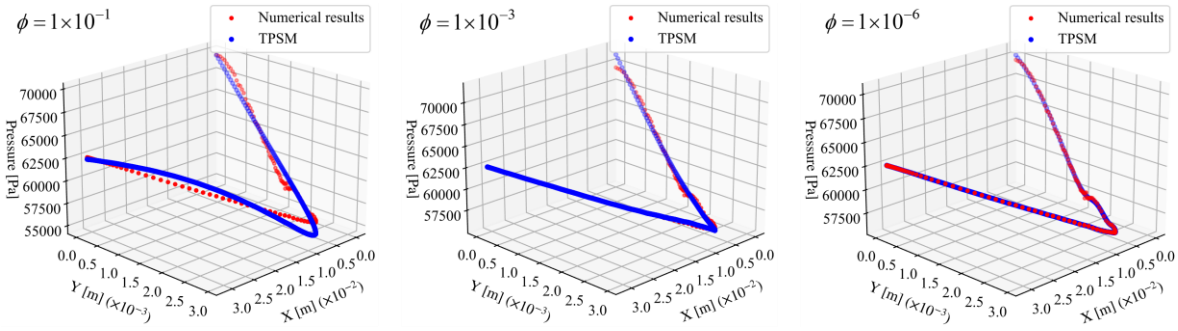


Fig. 6 Fitting performance of TPSM considering different interpolation coefficients.

4.3 Numerical solutions and discussions

Numerical simulations of ETDI are further carried out, with the heat flux density specified as $q_{in} = 13\mathrm{kW/m^2}$. The progressive contours of temperature and phase field are provided in Fig. 7(a), accompanied with water film profile at fracture constant. In the early stage of heating, thermal stresses generate at the bottom of ice layer, resulting in interfacial cracking prior to melting. As heating proceeds, water film forms in the heated region, leading to a pseudo “cracking healing” phenomenon induced by the crack driving threshold [18], as illustrated in Fig. 7(b). Eventually, a high stress concentration forms at the edge of phase transition zone, thereby causing through-cracking. The simulated results are also comparable with previous published ones, as illustrated in Fig. 7(c) and Fig. 7(d), respectively.

In addition, the ETDI results without including aerodynamic pressure are also presented in Fig. 8(a). Only interfacial cracking occurs, and the cracking proceeds more rapidly relative to the case with aerodynamic loads considered. This may be attributed to the fact that aerodynamic pressure restrains structural deformation, thereby reducing strain energy and delaying the crack propagation. As shown in Fig. 8(b), when phase fraction α reaches approximately 0.4 at the bottom, fully interfacial cracking has already taken place.

The above analysis preliminarily indicates that, when studying ETDI, the aerodynamic loads are supposed to be taken into account rather than oversimplified.

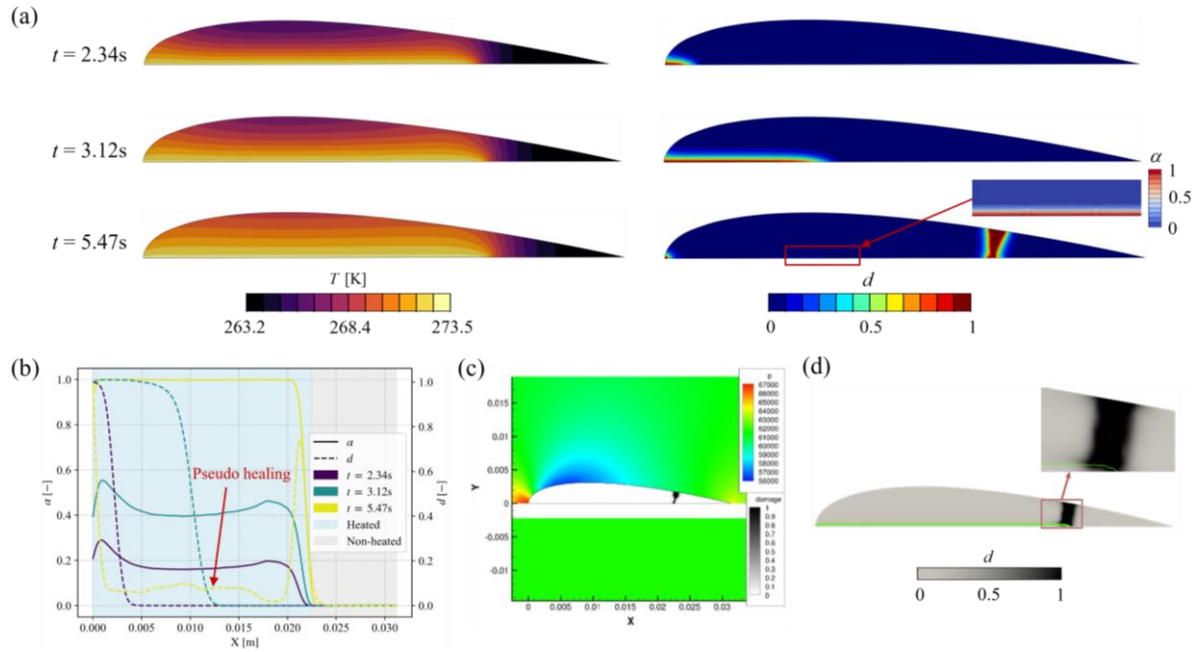


Fig. 7 ETDI results for idealized ice layer: (a) evolutions of temperature and phase field, (b) tempo-spatial distributions of phase field and phase fraction at the bottom edge, (c) derived from Bennani et al. [16], and (d) results obtained from Camberlin et al. [10].

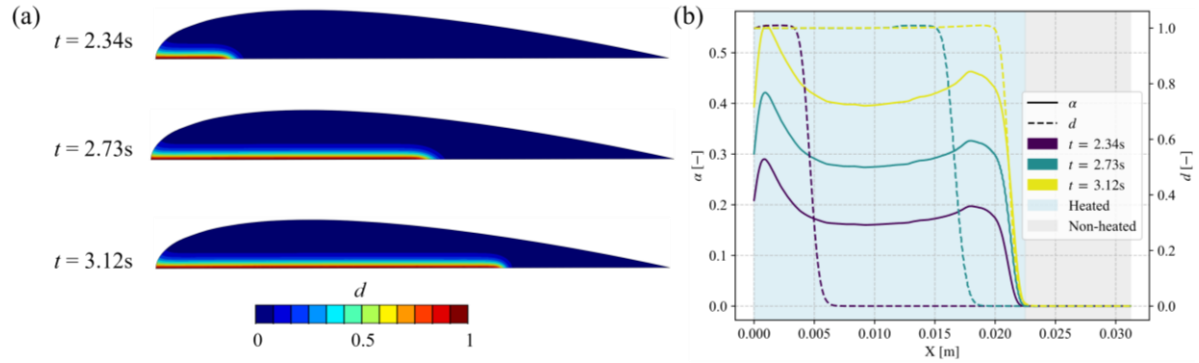


Fig. 8 ETDI results neglecting aerodynamic effects: (a) progressive phase field profiles, and (b) tempo-spatial evolutions of phase field and phase fraction at the bottom edge.

5. ETDI at NACA 0012 airfoil

5.1 Iced wing leading edge configuration

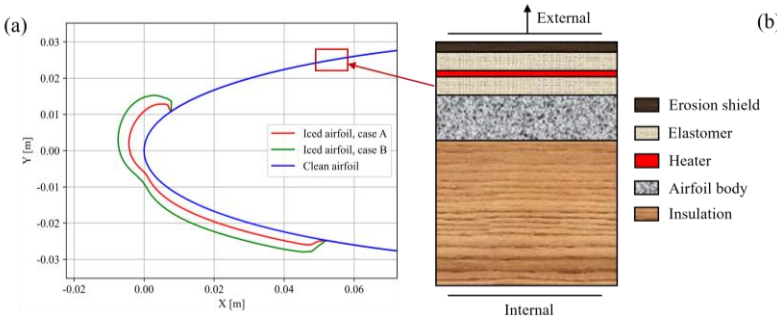
Upon validation cases, the above numerical framework is applied to study ETDI at NACA 0012 wing leading edge. The icing simulations are conducted in commercial software FENSAP-ICE, following the calculations of airflow field, droplet field and icing thermodynamics. The corresponding parameters are listed in Table 5. Two icing durations are considered, namely $t_{ice}=180\text{s}$ and $t_{ice}=360\text{s}$, which are designated as case A and case B respectively.

Table 5 Icing conditions under different exposure time.

Variable	Re	V_∞	T_∞	P_∞	*LWC**	*MVD**	AOA	t_{ice}*
Value	2.83×10^6	66.98	268.15	1.013×10^5	1.0	20.0	4	180 360
Unit	-	m/s	K	Pa	g/m^3	μm	°	s

Notes*: *LWC* denotes liquid water content; *MVD* is the median volume diameter of droplets; t_{ice} denotes the total icing time.

The icing simulation results are plotted in Fig. 9(a). With the extension of icing time, the mass and average thickness of ice accumulation on the airfoil are obviously increased. Besides, in engineering applications, heating pad is usually installed within the airfoil, and ice is removed via thermal conduction. Thus, a multi-layer structure is employed, as shown in Fig. 9(a). The materials and thermal properties of different layers [24,25] are summarized in Fig. 9(b).



(b)

Parameter	t_{thick}	k	C_p	ρ
Erosion shield	0.20	16.3	502.416	8025.25
Elastomer	0.28	0.256	1256.04	1384.2
Heater	0.013	41.0	385.186	8096.26
Airfoil body	0.89	0.294	1570.05	1794.1
Insulation	3.43	0.121	1130.44	648.75
Unit	mm	W/m/K	J/kg/K	kg/m^3

Fig. 9 Iced NACA 0012 wing leading edge: (a) ice shape and multi-layer structure, and (b) material parameters of different layers [24,25].

During numerical calculation, the wing leading edge is regarded as a rigid body, and its thermal expansion is neglected. In addition, aerodynamic pressure, formed by TPSM, is only applied on the outer surface of ice layer, and the convective heat transfer condition is considered for the whole external boundary.

5.2 ETDI results: comparison with experiments

In this section, $q_{in} = 9\text{kW/m}^2$ is specified. The phase field evolutions for case A and case B are summarized in Fig. 10, and regions where phase field value exceeds 0.95 are eliminated for better visualization. Under the action of thermal stresses, cracking first nucleates at the ice-airfoil interface, along with the formation of local water films. With continuous heating, the interfacial cracks converge toward the stagnation point. Driven by external aerodynamic loads, through-thickness crack eventually generates within the ice layer, leading to ice fracture and subsequent shedding. The de-icing time of case A is slightly shorter than that of case B, which may be attributed to a relative faster melting rate and a smaller ice thickness.

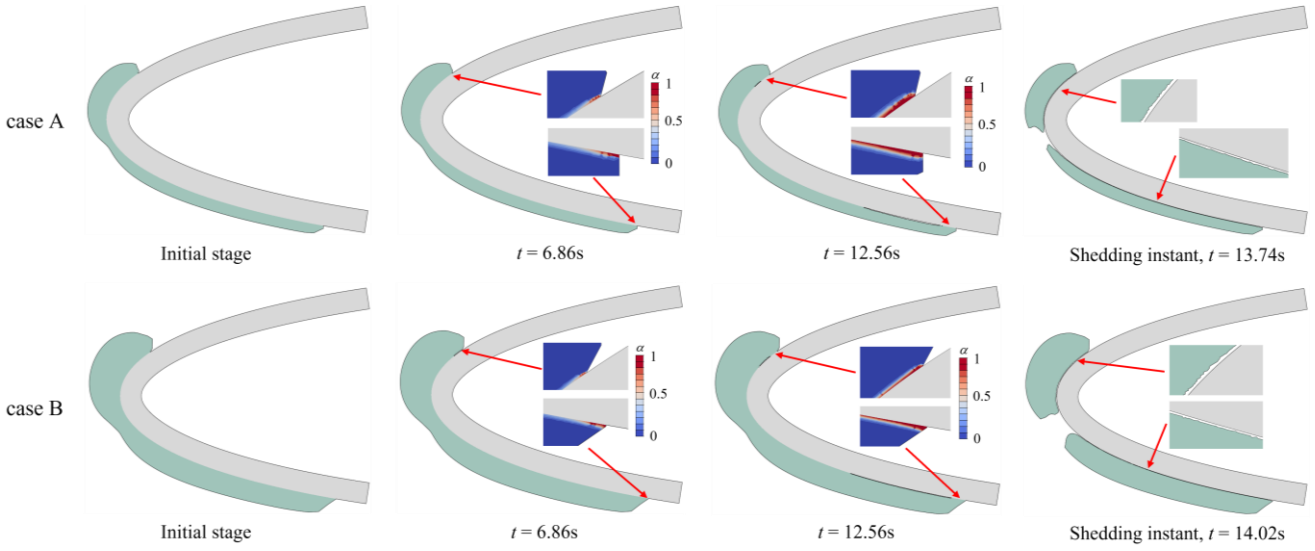


Fig. 10 Progressive phase field profiles for case A and case B.

The experimental results of ETDI in icing wind tunnel [26] are provided in Fig. 11. As mentioned, from the onset of heating shown in Fig. 11(a), mushy regions emerge at the ice-airfoil interface, corresponding to the phase transition as illustrated in Fig. 11(b). Eventually, Fig. 11(c) shows the completion of phase change, along with ice fracture and shedding (marked in blue) induced by aerodynamic forces. Despite being a qualitative comparison, experimental results still demonstrate the effectiveness of numerical ones to some degree.

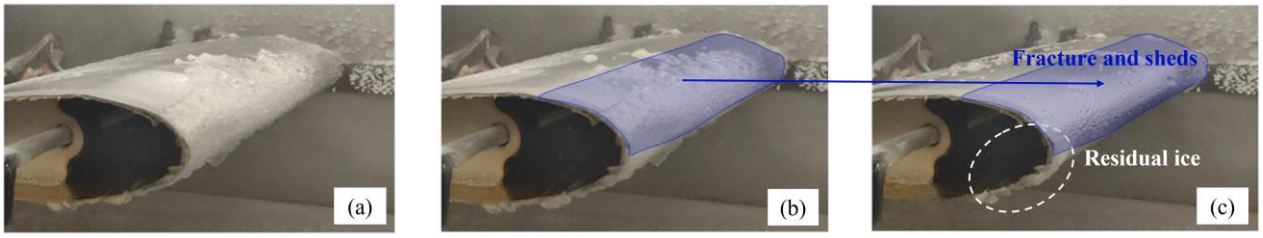


Fig. 11 Airfoil ETDI tests in icing wind tunnel [26].

As shown in Fig. 12(a), the maximum water film thickness $e_{\max}$, a time-dependent variable, can be regarded as an ice removal indicator. For instance, an empirical ETDI criterion claims that the ice can be removed once $e_{\max} > 0.2\text{mm}$ [27,28]. Thereby, the numerically obtained $e_{\max}$ is compared against the above empirical criterion, as demonstrated in Fig. 12(b). It can be found that, despite the difference in evolution laws, the water film thickness thresholds at the icing shedding moment for case A and case B are in good agreement with the empirical rule. This further confirms the reliability and effectiveness of the established ETDI model.

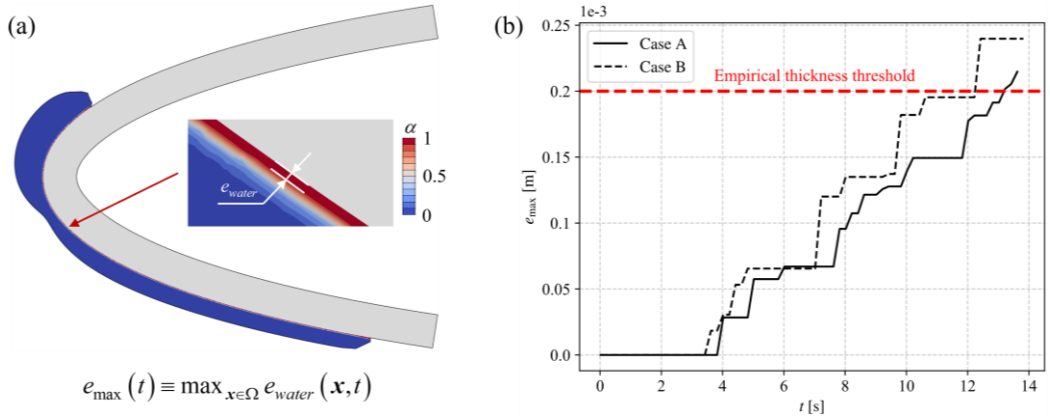


Fig. 12 Evolutions of maximum water film thickness: (a) illustrations, and (b) comparison with an empirical formula.

5.3 Effects of heating strategy

ETDI systems often face the challenge of excessive energy consumption. Hence, the ETDI behavior under different heat flux densities are investigated, with the energy consumption W_{ener} reads:

$$W_{ener} = t_{de} \cdot q_{in} \cdot S_a \,, \tag{20}$$

where t_{de} is the de-icing time, S_a represents the arc length on which the heat flux is applied.

Three heat flux densities, namely 4.5kW/m^2, 9kW/m^2 and 18kW/m^2, are adopted. The corresponding ice shedding behaviors are summarized in Fig. 13. Under varied heat flux densities, the ice shedding mode remains essentially unchanged, with both interfacial and penetrate cracking identified in all cases. Nevertheless, the area of through-thickness damage is markedly enlarged as q_{in} elevated, which is associated with the rapid variation of temperature gradient. In addition, a clear negative correlation between de-icing time and heat flux density can be found.

As presented in Fig. 14, the variations of energy consumption and water film thickness thresholds are compared. It can be concluded that the consumed energy decreases significantly with the increase in power density. This is consistent with the analysis of Pourbagian et al. [29], namely that rapid and energy-saving de-icing can be achieved by utilizing a “short-duration and high-power” heating mode. Besides, all numerical results of $e_{\max}$ are comparable in magnitude to 0.2mm, while it reveals discrepancies in thickness thresholds among distinct heating modes. This also demonstrates the potential to provide more precise criteria for different ETDI cases.

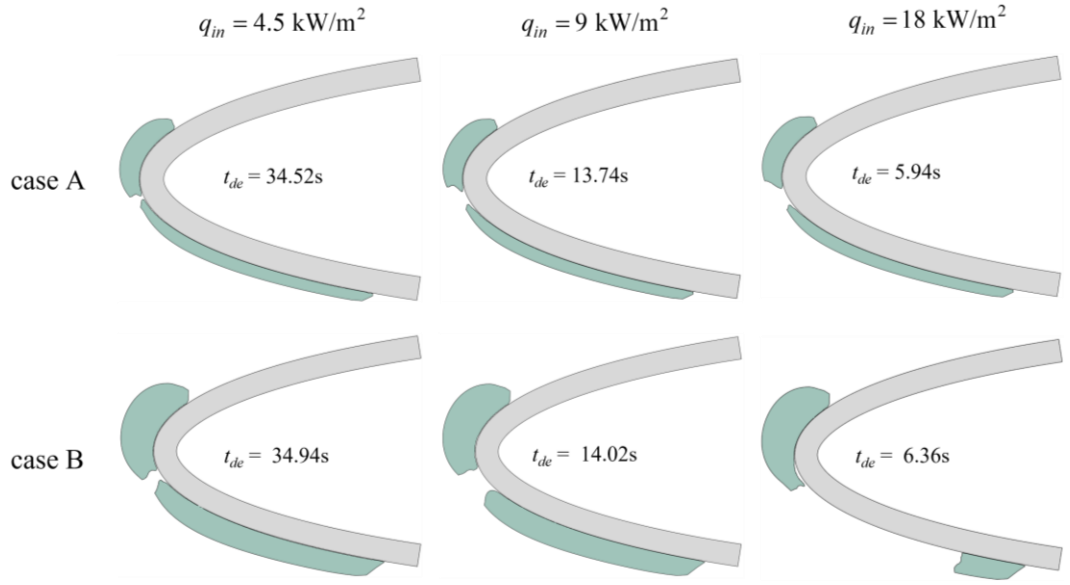


Fig. 13 ETDI behaviors under different heat flux densities.

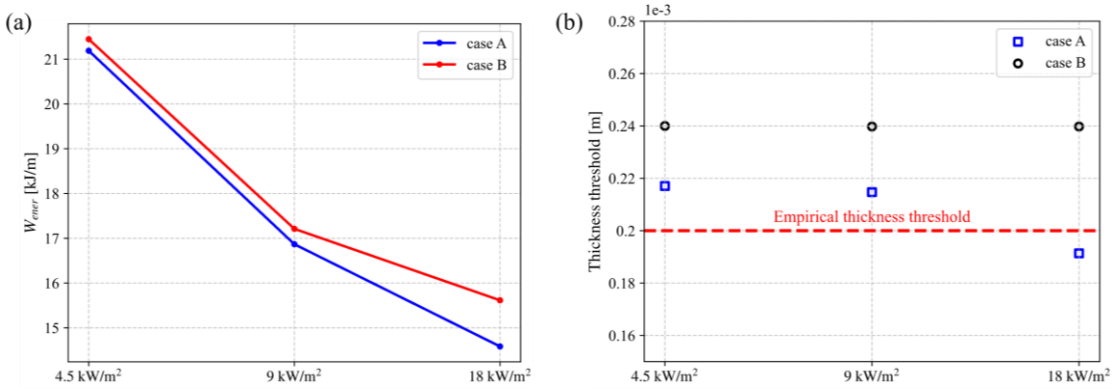


Fig. 14 Variations of important indicators during ETDI under different heating conditions: (a) energy consumption, and (b) maximum water film thickness threshold.

6. Conclusions and outlooks

In this study, a novel PFM accounting for solid-liquid transitions is applied to airfoil ETDI simulations. The TPSM is introduced to handle the aerodynamic load transfer caused by mismatched meshes at fluid-ice interface.

ETDI on an idealized ice layer is firstly conducted. Numerical solutions indicate that aerodynamic forces induce internal damage in the late stage of ETDI, while only interfacial cracking occurs when neglecting aerodynamic loads. Further ETDI simulations are carried out on NACA 0012 wing leading edge. The predicted ice fracture and shedding behavior fit well with the experimental results. It's also confirmed that the "short-duration and high-power" heating mode enables efficient de-icing while maintaining low energy expenditure, and the meltwater film thickness at ice shedding instant is in good agreement with a class of de-icing criterion. The above results illustrate the accuracy and effectiveness of proposed ETDI numerical model.

ETDI involves complex multi-physical process, and the inherent mechanisms remain to be further explored. For instance, due to the typical porous characteristics, meltwater may seep within the ice skeleton, resulting in a poro-elastic problem. Developing a corresponding thermo-hydro-mechanical PFM is vital for improving ETDI modeling.

7. Acknowledgements

The authors appreciate the supports from the National Natural Science Foundation of China (Grants No. 52302457).

8. Contact Author Email Address

To contact us, mailto:
Yuxuan Ying: yingyuxuan@mail.nwpu.edu.cn
Xudan Yao: x.yao@nwpu.edu.cn

9. Copyright Statement

The authors confirm that they, and/or their company or organization, hold copyright on all of the original material included in this paper. The authors also confirm that they have obtained permission, from the copyright holder of any third party material included in this paper, to publish it as part of their paper. The authors confirm that they give permission, or have obtained permission from the copyright holder of this paper, for the publication and distribution of this paper as part of the ICAS proceedings or as individual off-prints from the proceedings.

References

[1] Mu Z, Lin G, Shen X, et al. Numerical Simulation of Unsteady Conjugate Heat Transfer of Electrothermal Deicing Process. Int J Aerospace Eng. 2018; 1-16.
[2] Yao X, Hawkins SC, Falzon BG. An advanced anti-icing/de-icing system utilizing highly aligned carbon nanotube webs. Carbon. 2018; 136: 130-138.
[3] Yao X, Hawkins SC, Falzon BG. A repairable carbon nanotube web-based electro-thermal heater and damage sensor for aerospace applications. Aeronaut J. 2021; 125(1292): 1833-1843.
[4] Sloan J. 787 integrates new composite wing deicing system. Composites World, 2008.
[5] Nehls G. Embraer, Collins Aerospace demonstrate CNT-based ice protection system. Composites World, 2022.
[6] Esmaeilifar E, Raj LP, Myong R. Computational simulation of aircraft electrothermal de-icing using an unsteady formulation of phase change and runback water in a unified framework. Aerosp Sci Technol. 2022: 107936.
[7] Guo X, Yang Q, Zheng H, et al. Integrated composite electrothermal de-icing system based on ultra-thin flexible heating film. Appl Therm Eng. 2024; 121723.
[8] Chang S, Qi H, Deng H. Numerical investigation of airfoil ice accumulation: Ice shape and ice crack propagation. Eng Fract Mech. 2023; 281: 109081.
[9] Scavuzzo RJ, Chu ML, Ananthaswamy V. Influence of aerodynamic forces in ice shedding. J Aircraft. 1994; 31(3): 526-530.
[10] Camberlin E, Bennani L, Charlotte M, et al. A liquid-solid thermo-mechanical phase-field fracture model for electrothermal wing de-icing system. AIAA-2024-4071, 2024.
[11] Chen Y, Fu L, Dong W. Novel Cohesive/Adhesive Ice Shedding Model for Spinner Cone. J Propul Power. 2018; 34(3): 647-659.
[12] Nezzar D, Rannou J, Villedieu P, et al. Simulation of Ice Shedding From Rotating Parts Using Phase-Field Fracture and Cohesive Zone Models. AIAA Aviation Forum and Ascend, 2024.
[13] Francfort GA, Marigo JJ. Revisiting brittle fracture as an energy minimization problem. J Mech Phys Solids. 1998; 46(8): 1319-1342.
[14] Yin Y, Yu H. A thermodynamic-consistent phase-field model for fracture in temperature-dependent materials. Int J Mech Sci. 2025; 297-298: 110382.
[15] Clayton T, Duddu R, Sigert M, et al. A stress-based poro-damage phase field model for hydrofracturing of creeping glaciers and ice shelves. Eng Fract Mech. 2022; 272: 108693.
[16] Bennani L, Villledieu P, Salaun M, et al. Numerical simulation and modeling of ice shedding: Process initiation. Comput Struct. 2014; 142: 15-27.
[17] Bennani L, Villedieu P, Salaun M. A mixed adhesion-brittle fracture model and its application to the numerical study of ice shedding mechanisms. Eng Fract Mech. 2016; 158: 59-80.
[18] Ying Y, Feng Y, Huang W, et al. A thermo-mechanical phase field fracture model considering solid-liquid transition. Eng Fract Mech. 2026; 338: 112025.
[19] Miehe C, Welschinger F, Hofacker M. Thermodynamically consistent phase-field models of fracture: Variational principles and multi-field FE implementations. Int J Numer Meth Eng. 2010; 83(10): 1273-1311.
[20] Li W, Yang F, Fang D. The temperature-dependent strength model for ultra-high temperature ceramics.

Acta Mech Sinica Prc. 2010; 26(2): 235-239.

[21]Li D, Li P, Li W, et al. Three-dimensional phase-field modeling of temperature-dependent thermal shock-induced fracture in ceramic materials. Eng Fract Mech 2022; 268: 108444.

[22]Huang J, Li W, He Y, et al. Temperature-dependent tensile strength model for 2D woven fiber reinforced ceramic matrix composites. Compos Struct 2021; 267: 113890.

[23]Spalart PR, Allmaras SR. A One-Equation Turbulence Model for Aerodynamic Flows. AIAA Paper 92-0439, 1992.

[24]Al-Khalil KM, Horvath C, Miller DR, et al. Validation of NASA thermal ice protection computer codes. part 3: the validation of antice. Proceedings of the 35th Aerospace Sciences Meeting and Exhibit. 1997.

[25]Guo X, Yang Q, Zheng H, et al. Optimization of power distribution for electrothermal anti-icing systems by differential evolution algorithm. Appl Therm Eng. 2023; 221: 119875.

[26]Tang C, Yan Y, Wang R, et al. Experimental investigation on improving the electro-thermal efficiency of a novel GLARE leading-edge deicing structure. Aerosp Sci Technol. 2026; 175: 111881.

[27]Wang T, Zhang W, Chen J, et al. Power optimization of the aircraft electrothermal de-icing heaters. Appl Therm Eng. 2025; 280: 128236.

[28]Lei G, Dong W, Zhu J, et al. A new melting model in electrothermal de-icing simulation. In Proceedings of the ASME Turbo Expo 2015: Turbine Technical Conference and Exposition. Volume 5A: Heat Transfer, page V05AT10A009, Montreal, Quebec, Canada, 2015. ASME.

[29]Pourbagian M, Habashi W. CFD-based Optimization of Electro-Thermal Wing Ice Protection Systems in De-icing Mode. AIAA Aerospace Sciences Meeting Including the New Horizons Forum & Aerospace Exposition. 2013.